

Are patient specific meshes required for EIT head imaging?

This content has been downloaded from IOPscience. Please scroll down to see the full text.

2016 Physiol. Meas. 37 879

(<http://iopscience.iop.org/0967-3334/37/6/879>)

View [the table of contents for this issue](#), or go to the [journal homepage](#) for more

Download details:

IP Address: 128.41.61.111

This content was downloaded on 16/08/2016 at 14:32

Please note that [terms and conditions apply](#).

You may also be interested in:

[Correcting electrode modelling errors in EIT on realistic 3D head models](#)

Markus Jehl, James Avery, Emma Malone et al.

[Correction of electrode modelling errors in multi-frequency EIT imaging](#)

Markus Jehl and David Holder

[In vivo bioimpedance changes during haemorrhagic and ischaemic stroke in rats: towards 3D stroke imaging using electrical impedance tomography](#)

T Dowrick, C Blochet and D Holder

[Optimal choice of the regularization parameter for linear EIT of brain function](#)

Juan-Felipe P J Abascal, Simon R Arridge, Richard H Bayford et al.

[Modelling for imaging neuronal depolarization by electrical and magnetic detection impedance tomography](#)

O Gilad, L Horesh and D S Holder

[Comparison of frequency difference reconstruction algorithms for the detection of acute stroke using EIT in a realistic head-shaped tank](#)

B Packham, H Koo, A Romsauerova et al.

Are patient specific meshes required for EIT head imaging?

Markus Jehl, Kirill Aristovich, Mayo Faulkner
and David Holder

University College London, London WC1E 6BT, UK

E-mail: markus.jehl.11@ucl.ac.uk

Received 30 November 2015, revised 12 January 2016

Accepted for publication 14 January 2016

Published 20 May 2016



CrossMark

Abstract

Head imaging with electrical impedance tomography (EIT) is usually done with time-differential measurements, to reduce time-invariant modelling errors. Previous research suggested that more accurate head models improved image quality, but no thorough analysis has been done on the required accuracy. We propose a novel pipeline for creation of precise head meshes from magnetic resonance imaging and computed tomography scans, which was applied to four different heads. Voltages were simulated on all four heads for perturbations of different magnitude, haemorrhage and ischaemia, in five different positions and for three levels of instrumentation noise. Statistical analysis showed that reconstructions on the correct mesh were on average 25% better than on the other meshes. However, the stroke detection rates were not improved. We conclude that a generic head mesh is sufficient for monitoring patients for secondary strokes following head trauma.

Keywords: electrical impedance tomography, image reconstruction, head meshes, patient specific model

(Some figures may appear in colour only in the online journal)

1. Introduction

1.1. Background

Electrical impedance tomography (EIT) is a non-invasive three-dimensional medical imaging technology relying on a small, low cost device and is therefore of interest in many medical



Original content from this work may be used under the terms of the [Creative Commons Attribution 3.0 licence](https://creativecommons.org/licenses/by/3.0/). Any further distribution of this work must maintain attribution to the author(s) and the title of the work, journal citation and DOI.

diagnostic fields. Because of the ill-posed image reconstruction problem, small measurement noise and modelling errors introduce large artefacts into the images and can make detection of physiological changes impossible. In static imaging, where no baseline measurement is available, it has been shown that inaccurate head models have a detrimental effect on image quality (Kolehmainen *et al* 1997, Jehl *et al* 2015b). Therefore, most EIT applications use time-difference (TD) data, based on the observation that most geometric and system related errors cancel out when a reference measurement is subtracted from the data measurement (Brown 2003). TD applications of head EIT include the analysis of epileptic seizures (Bagshaw *et al* 2003) and imaging of cortical activity (Tidswell *et al* 2001), but the focus of this paper is the monitoring of patients with traumatic brain injury (TBI) for secondary bleeding (Xu *et al* 2010).

It has previously been found that even in TD, a head-shaped finite element model produces better images than spherical models (Bagshaw *et al* 2003). Based on this finding, ways have been investigated to create patient-specific head models based on either a computed tomography (CT) or a magnetic resonance imaging (MRI) scan of the head (Tizzard *et al* 2005, Vonach *et al* 2012). However, it has not yet been ascertained if differences between heads introduce enough errors into reconstructed images to justify the use of patient specific head meshes. If not, then images for studies of EIT of the adult head could all be undertaken with one anatomically accurate model of a generic head, which would represent a considerable saving in time and effort.

1.2. Purpose

The purpose of this work was to assess how accurately a human head has to be modelled to enable EIT monitoring and imaging. The questions to be answered were: (1) how large are voltage and image errors introduced by using a generic head mesh, as opposed to a subject specific one? (2) Is a subject specific head mesh required for the detection of localised conductivity changes?

These were addressed in computer simulation on accurate head meshes from MRI and CT scans of four patients' heads, created using a novel method. Two conductivity perturbations with different magnitude, haemorrhage and ischaemia, were chosen to test the reconstruction quality. Boundary voltages and Jacobian matrices were computed on all four meshes, for ischaemia or haemorrhage at five different locations. Time-difference images were then reconstructed from the simulated noisy boundary voltages, using the four different meshes and a coarse, homogeneous head model. Analysis of the resulting TD image quality—evaluated as the inverse of objective measures of image errors—showed that even though the image quality was generally better with the correct mesh, the number of correct perturbation detections was not higher than with the other head meshes and even the homogeneous mesh.

2. Mesh creation

The mesh generation pipeline used required a CT scan and an MRI scan of the same head, and the open source software suites Seg3D (CIBC 2015), MIPAV (McAuliffe *et al* 2001), CGAL (CGAL 2015) and MedInria (Toussaint *et al* 2007).

2.1. Segmentation

Previous head segmentations for EIT were based on either a CT scan and then morphing a brain into the shape of the skull (Vonach *et al* 2012), or on MRI scans with poor sensitivity to the skull shape (Tizzard *et al* 2005, Sadleir *et al* 2010, Vonach *et al* 2012). The method

proposed by Vonach *et al* (2012) did not allow for meshing of white matter or other tissues apart from brain, cerebrospinal fluid (CSF), skull and scalp. Also, it required that one tissue completely enclosed the inner one, which is not anatomically correct. The greatest difficulty in head segmentation for EIT is, however, the accurate modelling of the skull with respect to the soft tissues. The combination of the conductive scalp and highly resistive skull underneath means that a significant proportion of the injected current is shunted around the brain (Abascal *et al* 2008). For this reason, CT scans were used in this study for accurate skull segmentations and MRI scans of the same heads for soft tissue segmentation. The segmentation was mostly manual and took around two working days per head. In the following, the approximate procedure is described, with segmented layers printed in *italics* and Seg3D tools in CAPITALS (figure 1).

- CT and MRI head scans of the same patient were loaded into Seg3D. The rotational mismatch was estimated and the MRI scan was then rotated to align with the CT scan using MIPAV. Once the two scans were aligned, all segmentation work was done manually in Seg3D. The resolution of the CT and MRI scans was increased to $512 \times 512 \times 512$, using Gaussian interpolation (RESAMPLE tool). Increasing the number of pixels while smoothing the images was required to generate smooth surfaces in the resulting finite element meshes.
- The *skull* was segmented first by THRESHOLDING the CT scan at an appropriate intensity level (around one third of the maximum). The *diploë* was then found by FILLING HOLES in the *skull* and then REMOVING the *skull* from this newly created layer. The modelling of the diploë included anisotropy into the overall skull conductivity.
- The soft tissues were then extracted from the MRI scan. The first soft tissue to be segmented was the *white matter*, because it had a clearly visible contrast to the surrounding grey matter and could therefore be accurately found with the THRESHOLD tool (between around 40% and 50% intensity). Areas with similar intensity to the white matter were mostly outside the skull cavity, and could therefore be removed from the *white matter* by running REMOVE with the *skull* segmentation as the mask, and then finding CONNECTED COMPONENTS on the *white matter*.
- Next, the *grey matter* was found in a similar manner to the *white matter*. Because the grey matter MRI intensity (around 30–40%) was similar to tissues in the lower part of the head, it was generally not possible to disconnect the actual *grey matter* from the tissues with similar intensity by simply removing the *skull*. Therefore, this was done manually using the PAINT BRUSH tool to remove the connections between the *grey matter* and other tissues, based on physiological atlases. This was the most time-consuming step in the head segmentation.
- The *superior sagittal sinus* had a high intensity on the MRI scans (50–70%) and was easily segmented by THRESHOLDING and finding CONNECTED COMPONENTS. It was added to the *diploë* layer.
- By THRESHOLDING the MRI scan at very low intensity (below 10%), the *background* was segmented. At the nose and ears, the air filled cavities were manually removed (PAINT BRUSH) from the *background* and assigned to a new segmentation layer *air*. This was done, in order not to have highly irregular surfaces in the resulting finite element meshes.
- The *cerebrospinal fluid (CSF)* and *eyes* were combined to one layer, and found by thresholding the MRI scan at an intensity level of 10–20% and subsequent subtraction of *grey matter*, *white matter*, *skull* and *diploë* and *superior sagittal sinus*. Any unassigned gaps between *grey matter* and *skull* were filled with *CSF* by iteratively DILATING it and REMOVING the other layers to prevent overlap.

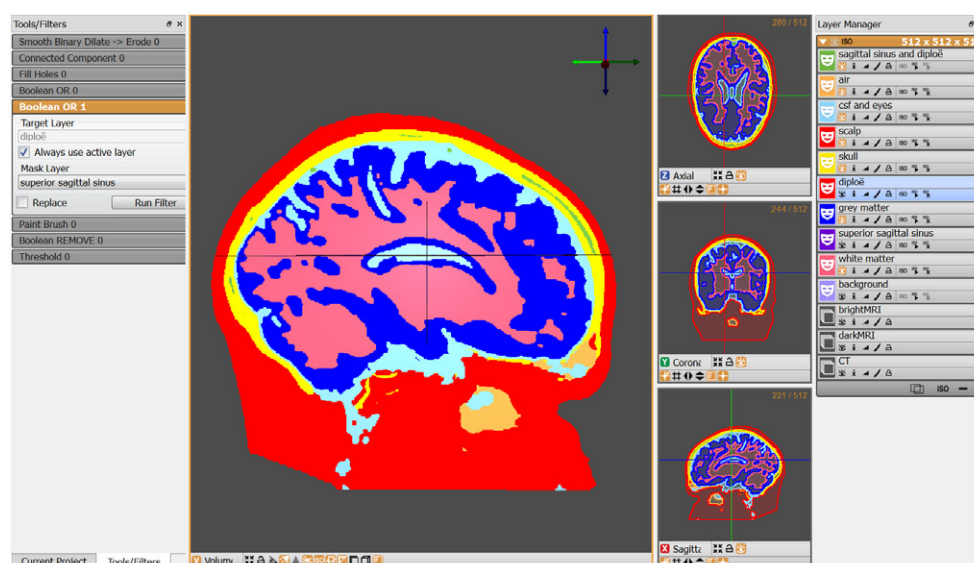


Figure 1. Screenshot of the Seg3D workspace after completed segmentation of CT and MRI scan. To the right are the created tissue layers and to the left the tools used.

- All unassigned voxels were finally assigned to a *scalp* layer, including most of the lower head, nose and throat. This simplification was deemed acceptable, because these areas were far from the electrodes and the region of interest (i.e. the brain). The *scalp* was found by THRESHOLDING the MRI to include all relevant tissues ($\sim 15\text{--}70\%$) and then subtracting all other segmented layers. DILATION and REMOVAL of the *background* ensured that the *scalp* covered the surface of the segmented head.
- When all tissue layers were segmented, they were smoothed by running SMOOTH BINARY DILATE \rightarrow ERODE and overlaps were prevented with BOOLEAN REMOVE. Finally, the segmentation was saved in .nrrd format and, using MedInria, translated into the .inr format required by the mesher.

2.2. Meshing

The high quality 3D mesh generator of the computational geometry algorithms library CGAL (CGAL 2015) was used to create tetrahedral meshes directly from the joint MRI&CT segmentation. The default 3D mesh generator of CGAL (written in C++) was adapted, by defining a problem specific element sizing field. This sizing field defined the desired finite element size throughout the head and was used to refine elements near the electrodes and towards the surface of the head. Specifically, all elements within a radius of 10 mm of the centre of an electrode were required to be 0.5 mm small, while the size of the other elements was assigned linearly from the surface to the centre of an ellipsoid fitted into the head (2 mm on the surface to 4 mm in the centre of the head). The effect of the mesh refinement around electrodes can be seen on the left of the slice taken of one head mesh, which cuts through an electrode located in posterior position (figure 2). The resulting meshes contained 3.3–3.5 million tetrahedral elements and their quality was controlled with the Joe-Liu quality measure (Liu and Joe 1994)

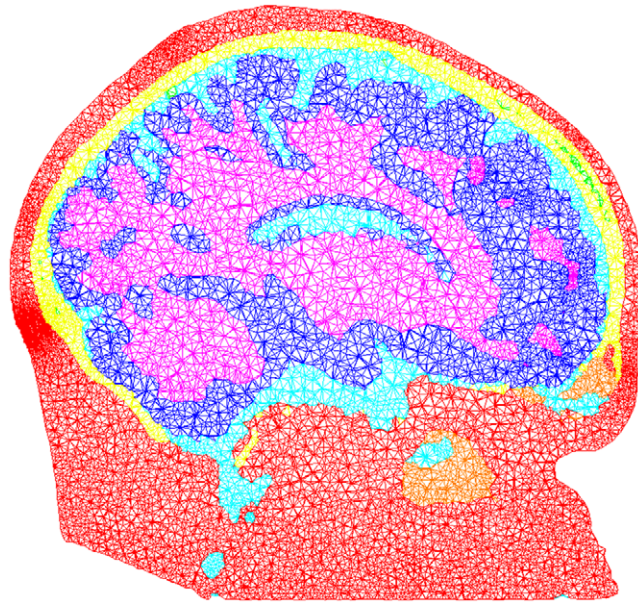


Figure 2. A slice through the 3D mesh created from the segmentation shown in Figure 1.

$$q = 12 \frac{(3V)^{\frac{2}{3}}}{\sum_{0 \leq i < j \leq 3} l_{ij}^2}, \quad (1)$$

where q is the quality, V the element volume and l the length of the edge between the i th and j th element vertex. All meshes had an average quality above 0.89 and not more than 7 elements with quality below 0.1 (with the worst element having a quality measure of 0.073).

After the manual location of nasion, inion and left and right ear tragus, the 32 electrode positions were computed automatically for each mesh using Matlab (MATLAB, The MathWorks, USA). The electrode positions were defined according to the EEG 10–10 system (Nuwer *et al* 1998) and matched the electrode assignment of the EasyCap EC40 (Brain Products GmbH, Germany). The head dimensions were analysed based on the distances between EEG 10–10 electrode positions Fpz and Oz (length), T7 and T8 (width) and the height was found as the difference between maximum and minimum z dimensions of nodes in the meshes (table 1). These head dimensions agree with anthropometric findings of an average head length of 188 ± 8.1 mm and an average head width of 145 ± 6.2 mm (Motmans and Ceriez 2005).

3. Methods

3.1. Voltage simulation

The conductivities σ of the used tissues were set to values compiled from literature for frequencies around 10 kHz (table 2; Horesh 2006). The current level was $250 \mu\text{A}$ and contact impedances of all 32 electrodes were $z_c = 1000 \Omega \cdot |E|$, with $|E|$ being the contact area of the electrodes with diameter 10 mm. The current injection pairs of electrodes were chosen to maximise the distance between electrodes by finding their maximum spanning tree. Measurements

Table 1. Dimensions of the four different heads used for meshing.

	Mesh 1	Mesh 2	Mesh 3	Mesh 4
Length	18.25	18.48	18.20	19.47
Width	14.89	15.52	15.19	15.07
Height	19.22	20.10	15.88	18.67

Note: all values are in centimetres.

Table 2. Used conductivity values for the modelled tissues, as compiled from literature by Horesh (2006).

Tissue	σ in S m^{-1}
Grey matter	0.15
White matter	0.3
CSF	1.79
Skull	0.018
Diploë and sagittal sinus	0.7
Air	0.0001
Scalp	0.44

were made for each injection on all adjacent electrode pairs not involved in delivering the current, giving a total of 869 measured voltages from 31 independent current injections. All voltages and the Jacobian matrix were computed with PERTS (Jehl *et al* 2015a), resulting in computation times of less than 11.5 min for voltages and Jacobian matrix on each healthy head model, and less than 3.5 min for the computation of only the voltages for each simulated stroke (on 12 processors with 20 MB cache each).

The five positions of the simulated perturbations were based on EEG 10–10 nomenclature electrode positions. Anterior, central and posterior were 25%, 50% and 75% along a line between Fpz and Oz, respectively. The lateral and superior positions were halfway between the central position and T8 and Cz, respectively. The simulated strokes had a radius of 1.5 cm and conductivity 0.7 S m^{-1} for haemorrhages and 90% of the healthy conductivity for ischaemias (Horesh 2006, Dowrick *et al* 2015).

Three levels of noise were added to simulated voltages and were chosen to match, in ascending order, tank experiments (Jehl *et al* 2015b), measurements on humans with relatively low noise and with higher noise (Goren *et al* 2015). This noise is referred to as *system noise*, and accounts for noise from the instrumentation. The noise levels were $\varsigma_p = 0.006\%$ proportional noise and $\varsigma_a = 1 \mu\text{V}$ additive noise, $\varsigma_p = 0.01\%$ & $\varsigma_a = 2 \mu\text{V}$ and $\varsigma_p = 0.02\%$ & $\varsigma_a = 5 \mu\text{V}$, such that

$$V_{\text{with noise}} = V_{\text{no noise}}(1 + \text{rand}(\varsigma_p)) + \text{rand}(\varsigma_a), \quad (2)$$

where $\text{rand}(\varsigma)$ indicates random numbers drawn from a Gaussian distribution with zero mean and standard deviation ς .

3.2. Image reconstruction

First order Tikhonov regularisation was used to bias the algorithm towards finding small connected perturbations (Lionheart *et al* 2004). All images were created with a standard least-squares minimisation using generalised singular value decomposition (gSVD). The advantage of using gSVD was that it only had to be computed once for each reconstruction mesh and

could then be used for all image reconstruction by simple matrix multiplication (Jehl *et al* 2015b).

To reduce the computational cost of calculating the gSVD and to prevent the ‘inverse crime’ (Lionheart *et al* 2004), much smaller hexahedral meshes (3–4 thousand elements of $1 \times 1 \times 1$ cm) were used for the image reconstructions. The Jacobian matrices were computed on the fine meshes and then projected onto the geometrically regular cubes of the hexahedral mesh. The Laplacian matrices for the first order Tikhonov regularisation were computed on the hexahedral meshes.

For all reconstructed images, the regularisation factor was kept constant for each noise level, and was $\lambda = 5 \times 10^{-4}$ for low noise, $\lambda = 1 \times 10^{-3}$ for medium noise and $\lambda = 2 \times 10^{-3}$ for high noise. The value for the lowest noise was chosen manually based on the shape of the L-curve (Hansen 1994). As the noise was roughly doubled, the regularisation factor was also doubled to account for the higher noise level. The colour bars of the images were scaled according to the largest reconstructed change in the whole mesh. Therefore images of slices sometimes do not contain the maximum value indicated in the colour bar.

3.3. Image and voltage error measures

Three metrics were used to objectively evaluate the image errors. These were error in location, and the ratio of background to perturbation, measured first as the average and then as the absolute sum of changes. All these were 0% in ideal images. The overall error was expressed as the sum of these three metrics in percent, and image quality as its reciprocal. Acceptable quality images were empirically found to have <100% image error or >0.01 image quality, respectively.

The volume P corresponding to the reconstructed perturbation was identified as the largest connected cluster of voxels with at least 75% of the maximum absolute change in the image (Jehl *et al* 2015b). The region of interest (ROI) was defined as the largest connected cluster of voxels with 50% of the maximum of the simulated conductivity change. The used error metrics were then

- Location error: ratio between the distance $\|(x_P, y_P, z_P)\|$ of the centre of mass of the reconstructed perturbation P from the actual perturbation location, and the average dimension of the mesh mean (d_x, d_y, d_z)

$$\frac{\|(x_P, y_P, z_P)\|}{\text{mean}(d_x, d_y, d_z)}. \tag{3}$$

- ROI contrast: ratio between the average reconstructed change $(d\sigma_r)$ outside the region of interest and the average reconstructed change in the region of interest

$$\frac{|\text{mean}_{\Omega \setminus \text{ROI}}(d\sigma_r)|}{|\text{mean}_{\text{ROI}}(d\sigma_r)|}. \tag{4}$$

- ROI noise: ratio between the absolute changes outside the region of interest and the absolute changes within the ROI

$$\frac{\text{mean}_{\Omega \setminus \text{ROI}}(|d\sigma_r|)}{\text{mean}_{\text{ROI}}(|d\sigma_r|)}. \tag{5}$$

The overall image quality was then defined as the inverse of the sum of the three error measures in percent (e.g. the image quality for 10% location error, 5% ROI contrast error and 25% ROI noise would be $1/(10 + 5 + 25) = 0.025$). Examples of image reconstructions with

differently assessed quality illustrate that up to 100% image errors it was possible to detect the stroke visually (figure 3). Between 100–120% some strokes could still be seen, while others could not. If the image errors were larger than 120%, it was no longer possible to detect strokes. 100% image errors were therefore defined as the limit of stroke detectability. The occurrence of a reconstruction with more than 120% was highlighted in tables 3 and 4 by colouring the entry red.

Voltage errors between two measurements $\mathbf{v}_1 - \mathbf{v}_2$ were assessed with two metrics. The 2-norm was computed as $(\sum_i (\mathbf{v}_1 - \mathbf{v}_2)_i^2)^{1/2}$ and the average proportional errors as $\text{mean}_i(|\mathbf{v}_1 - \mathbf{v}_2|/|\mathbf{v}_1|)$, where $i = 1, \dots, 869$ indexes the individual measured voltages.

4. Results

4.1. Analysis of the image quality

4.1.1. Was the image quality better with the correct mesh? For reconstruction on the correct mesh, the image quality metric was on average 25% better, than when different meshes were used for simulation and reconstruction. Sometimes, image reconstructions on the wrong mesh were better than reconstructions on the correct mesh. The image quality of reconstructions on the correct mesh was plotted against the average image quality of reconstructions on the other three head meshes (figure 4). For low noise, the improved quality using the correct mesh is clearly visible (blue crosses). The difference in image quality between correct mesh and other mesh reconstructions reduces with increasing noise. When filtering out reconstructions that were unsuccessful in both modalities (i.e. quality below $1/100\% = 0.01$ for both), then the following ratios of better reconstruction with the correct mesh versus better reconstruction with the other meshes were obtained: 32 : 8 at low noise, 22 : 16 at medium noise and 20 : 10 at high noise. An example of a reconstructed image on the correct mesh and the same reconstruction on a different mesh is shown in figure 5.

4.1.2. Were stroke detection rates higher with the correct mesh? While using the correct mesh for reconstruction increased image quality on average, the total amount of successful stroke detections was not improved (figure 4). The number of cases where reconstructions with the correct mesh were successful, while reconstructions with the wrong meshes were not, was 3 (all at the highest noise level). On the other hand, there were 5 cases where only the reconstructions on the wrong meshes gave an acceptable image quality (2 at the highest noise level, 1 at medium noise and 2 at low noise).

4.1.3. Which factors did stroke detection rates depend on? In this section, we compare the influence of mesh differences, stroke position, stroke type and system noise level on stroke detection rates. The system noise was found to have the strongest impact on image quality, and mostly affected reconstructions of ischaemia.

No clear differences were found between the meshes used for voltage simulation and image reconstruction (table 3). The only surprise was, that even at the highest noise level, almost all reconstructions from voltages simulated on mesh 1 were successful. No explanation was found for this observation. The least successful reconstructions of haemorrhages were observed for the posterior position, while the lateral position was the least successful for ischaemia recovery (table 4). The added system noise had a very strong influence on the successful reconstructions of ischaemic strokes. At the medium noise level, 66 out of 80 ischaemias were detected, while with the highest noise this number dropped to 33 (table 4).

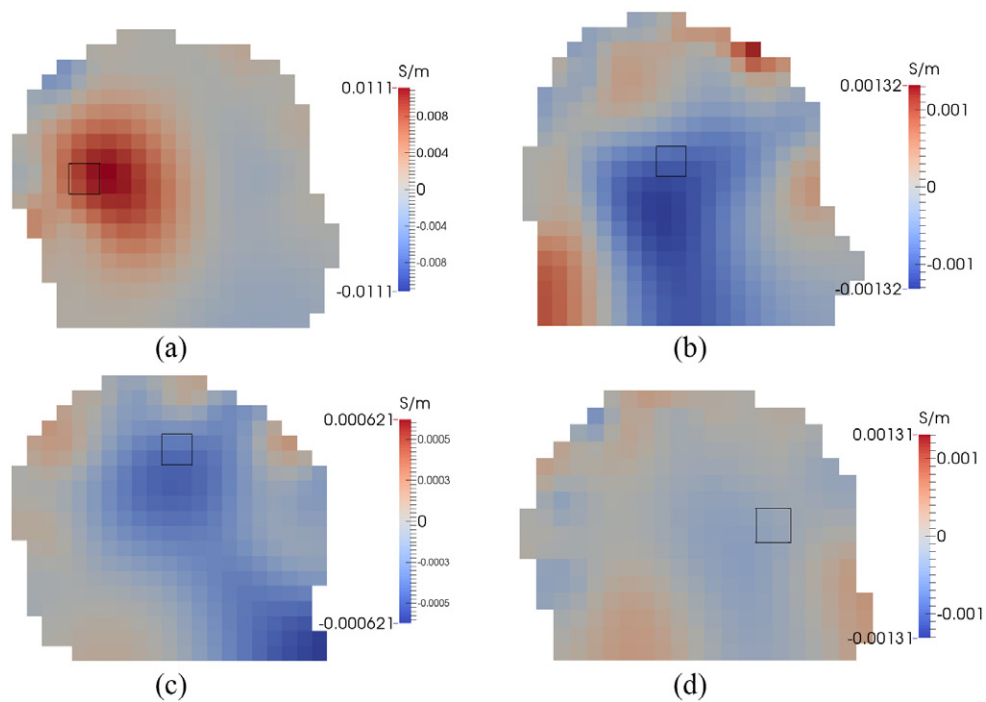


Figure 3. Illustration of image quality measures: (a) haemorrhage with 20% image errors, (b) ischaemia with 61% image errors, (c) 105% image errors and (d) 108% image errors. Black squares indicate the outline of the simulated stroke, thresholded at 50% of the maximum conductivity change in the hexahedral mesh.

Table 3. Number of successful reconstructions using different voltage simulation and image reconstruction mesh pairs.

		Simulation			
		Mesh 1	Mesh 2	Mesh 3	Mesh 4
Reconstruction	Mesh 1	9/9/9	10/8/6	10/8/5	10/8/5
	Mesh 2	8/9/10	9/10/5	10/10/5	9/8/4
	Mesh 3	10/9/10	10/10/7	10/9/7	10/9/5
	Mesh 4	10/9/10	10/10/7	10/9/8	10/9/6
	h.100 k	10/8/8	10/8/5	10/8/8	9/8/9

Note: the first value of each entry corresponds to small noise on the voltages, the second to medium noise and the last to high noise. The maximum score for each noise level is 10, which means that all five positions and both stroke types were visible in the reconstructed image. 0–100% image error were considered successful and everything above unsuccessful. If all images had an error of less than 120% the number is black, otherwise red. The last row corresponds to reconstructions on a coarse, homogeneous mesh.

Out of curiosity, time-difference reconstructions were also made on a coarse 100 thousand element head mesh with homogeneous conductivity of 0.3 S m^{-1} (last row of table 3). Surprisingly, most of these reconstructions were still good enough to identify the stroke, suggesting that TD reconstructions are more stable to geometrical errors than previously thought (Bagshaw *et al* 2003).

Table 4. Number of successful reconstructions using different noise levels and stroke positions.

		Noise level		
		0.006% & 1 μ V	0.01% & 2 μ V	0.02% & 5 μ V
Position	Posterior	16/16	14/15	13/8
	Central	16/15	16/15	16/7
	Anterior	16/14	16/15	16/7
	Superior	16/14	16/5	16/4
	Lateral	16/16	16/16	16/7

Note: the first value corresponds to haemorrhage, the second to ischaemia. The maximum score for each stroke type is 16, which means that all combinations of voltage simulation and image reconstruction meshes resulted in a good image. 0–100% image error were considered successful and everything above unsuccessful. If all images had an error of less than 120% the number is black, otherwise red.

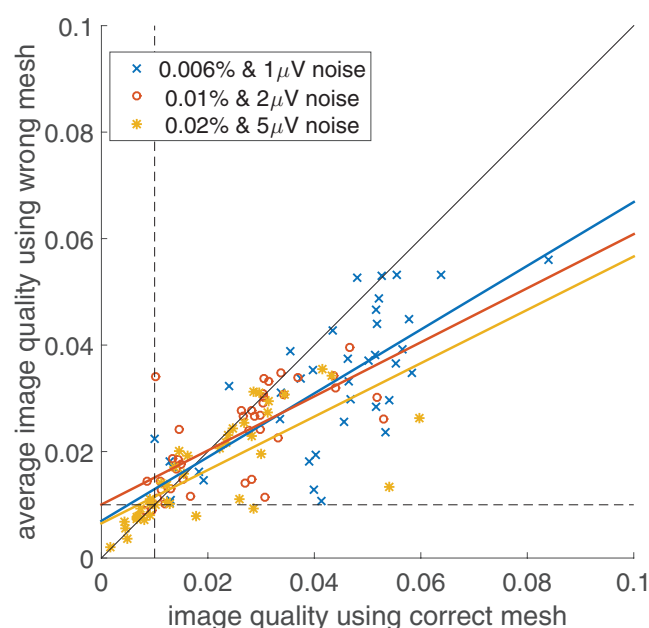


Figure 4. Image quality comparison for reconstructions on correct mesh and on different head meshes. The solid lines are the linear fit of the data points with the same colour. For each noise level there are 40 data points, corresponding to four meshes used for simulation, five stroke positions and two stroke types.

4.2. Analysis of the voltage errors

4.2.1. How large were voltage changes caused by the perturbations? The average 2-norm of the voltage change caused by haemorrhages was 301 μ V (1.3% proportional) and for ischaemias 27 μ V (0.1% proportional). These values were obtained by averaging the changes of the respective stroke types for all five positions. The position of the stroke had only a small influence on the signal. The largest changes were caused by posterior strokes, and were approximately 1.5 times larger than the smallest changes, which were caused by central strokes.

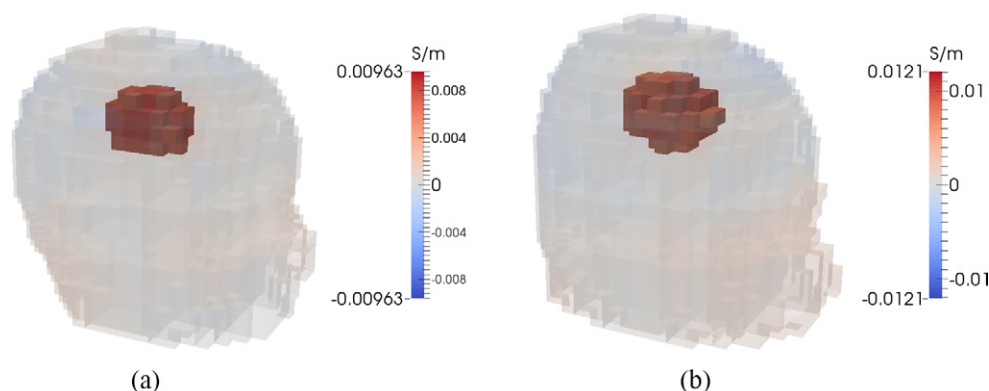


Figure 5. Example of reconstructions of a haemorrhage in the superior position simulated on mesh 1 and reconstructed on (a) mesh 1 and (b) mesh 2. The images were thresholded at 66% of the maximum reconstructed change.

4.2.2. How large were voltage errors introduced by wrong meshes? Baseline voltage differences were compared between all four head meshes, and the average for these six comparisons was computed. The average voltage differences were large with 2-norms between 16–35 mV (59–100% proportional).

Time-difference voltage changes were compared between all four head meshes for perturbations simulated in posterior position. The average TD voltage differences were 146 μV (0.63% proportional) for haemorrhage and 13 μV (0.07% proportional) for ischaemia.

4.2.3. How did this compare to the introduced system noise? The average 2-norm of the added proportional and additive noise was 28 μV (5.6% proportional) for low noise, 59 μV (11.3% proportional) for medium noise and 148 μV (28.3% proportional) for the highest used noise level. These values were computed based on the noise added to the baseline. Consequently, time-difference data contained a combination of the noise on the baseline and equivalent noise on the perturbation voltages.

4.2.4. Comparison of the voltage differences. In time-difference imaging, the geometrical errors were in the same range as the signal. On the other hand, the proportional and additive noise added to the simulated voltages was 2–10 times smaller than the haemorrhagic signal. This means that reconstructions of haemorrhagic strokes had a ten times better signal to system noise ratio than reconstructions of ischaemic strokes, while the signal to mesh difference ratios were comparable (figure 6).

Successful reconstructions of ischaemic strokes reduced strongly between medium and high system noise. The 2-norm of the signal was two times smaller than the 2-norm of the medium noise, suggesting this ratio as a good rule of thumb for estimating feasibility of head EIT applications.

5. Discussion

5.1. Mesh creation

The created head meshes were anatomically more accurate than previous EIT head models, due to the use of both CT and MRI scans, instead of just one of the two (Tizzard *et al* 2005,

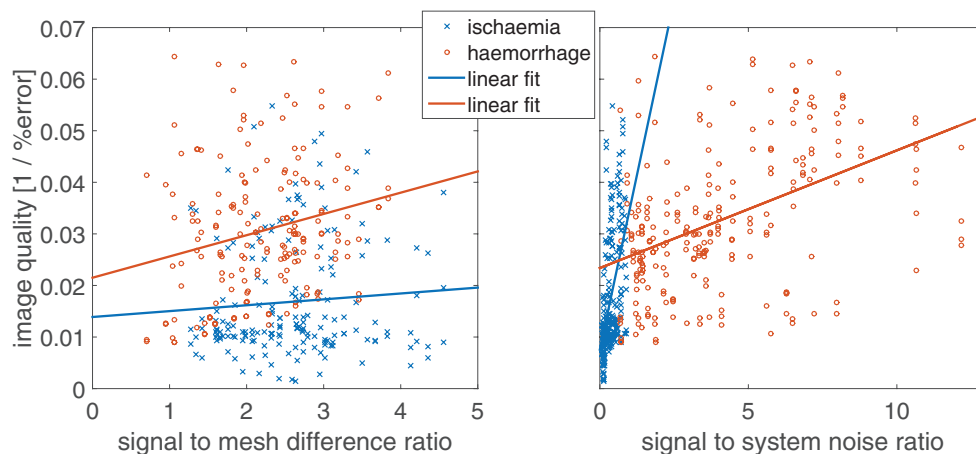


Figure 6. The plot on the left shows the effects of using a generic head mesh for reconstructions. The signal to mesh difference ratio was computed as the 2-norm of the voltage changes caused by the simulated stroke, divided by the 2-norm of the difference in time-difference voltage changes on the mesh used for voltage simulation and the mesh used for reconstruction. The plot on the right shows the image quality with respect to signal to system noise ratio for both types of stroke. For each stroke type there are 240 data points, corresponding to four meshes used for simulation, four meshes used for reconstruction, five stroke positions and three noise levels. However, the signal to mesh difference ratio was infinite if the same mesh was used for simulation and reconstruction, which is why only 180 data points for each stroke type are visible on the left plot.

Vonach *et al* 2012). The quality of the meshes was further improved by using the established open source CGAL mesh generator directly on the segmentation, thereby skipping previously required separate steps of enclosed 3D surface generation and meshing (Vonach *et al* 2012). Problem specific element sizing fields were defined to reduce element size near the electrodes, where electric potential gradients were large. Once the manual CT and MRI segmentations were performed, meshes with variable element sizes could be efficiently created by simply varying the CGAL settings in a text file.

5.2. Impact of mesh differences

Voltage differences between meshes, voltage changes caused by the simulated perturbations and the degree of added system noise were quantified by the 2-norm. The image quality of the reconstructions was assessed objectively by predefined metrics and a limit of detectability was set at 100% image errors. From these objective measures, the following answers were found to the questions posed at the beginning:

- (1) *How large are voltage and image errors introduced by using a generic head mesh, as opposed to a subject specific one?* Time-difference voltage errors between head meshes were of the same order than voltage changes caused by the perturbations. The image quality was on average 25% better, when the reconstructions were made on the correct mesh. When the added system noise was more than twice as high as the signal, then the stroke detection rate decreased significantly.
- (2) *Is a subject specific head mesh required for the detection of localised conductivity changes?* While using the correct mesh for reconstructions improved the overall image

quality, stroke detection rates were not improved. In three cases, only the correct mesh lead to a correct stroke identification, while there were five cases, where the reconstruction on the correct mesh failed and the average image errors on the other meshes were below 100%.

Finally, it was observed that even a coarse, homogeneous reconstruction mesh resulted in an acceptable image quality in most cases.

5.3. Conclusions

For monitoring, it was found not to be essential to use patient specific head meshes for image reconstructions. The results of this study, however, suggest that the noise on the measured voltages has to be kept very low to enable reliable detection of small conductivity changes in the head, such as ischaemia, epileptic seizures or even fast neural activity. Ways in achieving this may include long averaging, correction of small electrode movements (Jehl *et al* 2015b) and reduction of system errors (Fitzgerald *et al* 2002).

An EIT head imaging application in which it is very unlikely to have access to patient specific head meshes, is the differentiation of acute ischaemic and haemorrhagic strokes (Holder and Tidswell 2004). Since a baseline measurement is not available in this case, time-difference (TD) reconstructions are not available and multi-frequency (MF) methods have to be used (Malone *et al* 2014a). Previous results and preliminary work suggest that MF reconstructions are more sensitive to geometrical errors than TD (Malone *et al* 2014b), but more analysis needs to be done to give a definitive answer, whether patient-specific meshes are required in MF imaging.

This work suggests that monitoring the development of cerebral ischaemia or haemorrhage over time may be possible. This could be of clinical benefit following stroke thrombolysis, sub-arachnoid haemorrhage or head injury. For such studies, our recommendation based on this work is: construction of the Jacobian matrix with an accurate three million element mesh of a generic head and reconstruction on either the same mesh or a coarser hexahedral mesh.

Acknowledgments

The authors acknowledge the support of Neurology and Neurosurgery Queen's Square, University College London NHS Foundation Trust.

References

- Abascal J, Arridge S, Atkinson D, Horesh R, Fabrizi L, De Lucia M, Horesh L, Bayford R and Holder D 2008 Use of anisotropic modelling in electrical impedance tomography: description of method and preliminary assessment of utility in imaging brain function in the adult human head *NeuroImage* **43** 258–68
- Bagshaw A, Liston A, Bayford R, Tizzard A, Gibson A, Tidswell A, Sparkes M, Dehghani H, Binnie C and Holder D 2003 Electrical impedance tomography of human brain function using reconstruction algorithms based on the finite element method *NeuroImage* **20** 752–64
- Brown B 2003 Electrical impedance tomography (EIT): a review *J. Med. Eng. Technol.* **27** 97–108
- CGAL 2015 Computational geometry algorithms library (www.cgal.org)
- CIBC 2015 Seg3d: volumetric image segmentation and visualization. Scientific Computing and Imaging Institute (SCI) (www.seg3d.org)

- Dowrick T, Blochet C and Holder D 2015 In vivo bioimpedance measurement of healthy and ischaemic rat brain: implications for stroke imaging using electrical impedance tomography *Physiol. Meas.* **36** 1273–82
- Fitzgerald A, Holder D, Eadie L, Hare C and Bayford R 2002 A comparison of techniques to optimize measurement of voltage changes in electrical impedance tomography by minimizing phase shift errors *IEEE Trans. Med. Imaging* **21** 668–75
- Goren N, Avery J and Holder D 2015 Feasibility study for monitoring stroke and TBI patients *Proc. of 16th Int. Conf. on Biomedical Applications of Electrical Impedance Tomography* ed J Solà et al p 71
- Hansen P 1994 Regularization tools: a matlab package for analysis and solution of discrete ill-posed problems *Numer. Algorithms* **6** 1–35
- Holder D and Tidswell T 2004 *Electrical Impedance Tomography: Methods, History and Applications* ed D Holder (London: Taylor and Francis) chapter 4 pp 127–66
- Horesh L 2006 Some novel approaches in modelling and image reconstruction for multi frequency electrical impedance tomography of the human brain *PhD Thesis* University College London
- Jehl M, Dedner A, Betcke T, Aristovich K, Klöfkorn R and Holder D 2015a A fast parallel solver for the forward problem in electrical impedance tomography *IEEE Trans. Biomed. Eng.* **62** 126–37
- Jehl M, Avery J, Malone E, Holder D and Betcke T 2015b Correcting electrode modelling errors in EIT on realistic 3D head models *Physiol. Meas.* **36** 2423–42
- Kolehmainen V, Vauhkonen M, Karjalainen P and Kaipio J 1997 Assessment of errors in static electrical impedance tomography with adjacent and trigonometric current patterns *Physiol. Meas.* **18** 289–303
- Lionheart W, Polydorides N and Borsic A 2004 *Electrical Impedance Tomography: Methods, History and Applications* ed D S Holder (London: Taylor and Francis) chapter 1 pp 3–64
- Liu A and Joe B 1994 Relationship between tetrahedron shape measures *BIT Numer. Math.* **34** 268–87
- Malone E, Sato Dos Santos G, Holder D and Arridge S 2014a Multifrequency electrical impedance tomography using spectral constraints *IEEE Trans. Med. Imaging* **33** 340–50
- Malone E, Jehl M, Arridge S, Betcke T and Holder D 2014b Stroke type differentiation using spectrally constrained multifrequency EIT: evaluation of feasibility in a realistic head model *Physiol. Meas.* **35** 1051–66
- McAuliffe M, Lalonde F, McGarry D, Gandler W, Csaky K and Trus B 2001 Medical image processing, analysis and visualization in clinical research *Proc. 14th IEEE Symp. on Computer-Based Medical Systems (CBMS)* pp 381–6
- Motmans R and Ceriez E 2005 DinBelg 2005: body dimensions of the Belgian population (www.dinbelg.be/)
- Nuwer M, Comi G, Emerson R, Fuglsang-Frederiksen A, Guérit J M, Hinrichs H, Ikeda A, Luccas F and Rappelsburger P 1998 IFCN standards for digital recording of clinical EEG *Electroencephalogr. Clin. Neurophysiol.* **106** 259–61
- Sadleir R, Vannorsdall T, Schretlen D and Gordon B 2010 Transcranial direct current stimulation (tDCS) in a realistic head model *NeuroImage* **51** 1310–8
- Tidswell T, Gibson A, Bayford R and Holder D 2001 Three-dimensional electrical impedance tomography of human brain activity *NeuroImage* **13** 283–94
- Tizzard A, Horesh L, Yerworth R, Holder D and Bayford R 2005 Generating accurate finite element meshes for the forward model of the human head in EIT *Physiol. Meas.* **26** 251–61
- Toussaint N, Souplet J and Fillard P 2007 MedINRIA: medical image navigation and research tool by INRIA *Proc. of Medical Image Computing and Computer-Assisted Intervention* vol 7
- Vonach M, Marson B, Yun M, Cardoso J, Modat M, Ourselin S and Holder D 2012 A method for rapid production of subject specific finite element meshes for electrical impedance tomography of the human head *Physiol. Meas.* **33** 801–16
- Xu C, Wang L, Shi X, You F, Fu F, Liu R, Dai M, Zhao Z, Gao G and Dong X 2010 Real-time imaging and detection of intracranial haemorrhage by electrical impedance tomography in a piglet model *J. Int. Med. Res.* **38** 1596–604